

A&A manuscript no.
(will be inserted by hand later)

Your thesaurus codes are:
06 (03.09.7; 08.03.4; 08.09.1; 08.09.2; 08.23.3)

**ASTRONOMY
AND
ASTROPHYSICS**
October 31, 2018

Adaptive Optics imaging of P Cyg in H_{α} *

Chesneau O.¹, Roche M.², Boccaletti A.³, Abe L.¹, Moutou C.⁴, Charbonnier F.⁵, Aime C.², Lantéri H.², and Vakili F.¹

¹ Observatoire de la Côte d'Azur, Département Fresnel, GI2T, F-06460 Saint Vallier de Thiey

² UMR 6525 Astrophysique, Université de Nice Sophia Antipolis Parc Valrose, F-06108 Nice cedex 2

³ Collège de France, 11 Pl. M. Berthelot F-75321 Paris

⁴ European Southern Observatory, Alonso de Cordoba 3107, Santiago, Chile

⁵ Office National d'Etudes et de Recherches Aérospatiales, Département d'Optique Théorique et Appliquée Imagerie Haute Résolution - Optique Adaptative, 29 Av de la Division Leclerc, F-92320 Chatillon

Received January 10; accepted March 20, 2000

Abstract. We obtained H_{α} diffraction limited data of the LBV star P Cyg using the ONERA Adaptive Optics (AO) facility BOA at the OHP 1.52m telescope on October 1997. Taking P Cyg and the reference star 59 Cyg AO long exposures we find that P Cyg clearly exhibits a large and diffuse intensity distribution compared to the 59 Cyg's point-like source. A deconvolution of P Cyg using 59 Cyg as the Point Spread Function was performed by means of the Richardson-Lucy algorithm. P Cyg clearly appears as an unresolved star surrounded by a clumped envelope. The reconstructed image of P Cyg is compared to similar spatial resolution maps obtained from radio aperture synthesis imaging. We put independent constraints on the physics of P Cyg which agree well with radio results. We discuss future possibilities to constrain the wind structure of P Cyg by using multi-resolution imaging, coronagraphy and long baseline interferometry to trace back its evolutionary status.

Key words: star: P Cyg, techniques: adaptive optics, deconvolution

1. Introduction

Among the galactic Luminous Blue Variables (LBV), the supergiant P Cyg (HD 193237, B1Ia+) is both a historical prototype since its famous XVIIth century eruptions, and an intriguing paradigm in many aspects. In their exhaustive study of P Cyg's fundamental parameters, mass loss physics and evolution, Nota et al. (Nota et al. 1995) have held this star being the unique case of the so-called "Peculiar Nebulae" class LBVs. Indeed the 22 arcseconds (arcsec) faint and spherical nebulae around P Cyg were only recently discovered by Barlow et al. (Barlow et al. 1994)

Send offprint requests to: Chesneau O.

* Based on data collected at the Observatoire de Haute-Provence

Correspondence to: chesneau@astro.umontreal.ca

who estimate its mass as 0.01 solar mass. This value significantly differs from those of more regular LBVs, ranging from $1M_{\odot}$ to $4.2M_{\odot}$ (e.g. for AG Car) which also present more asymmetric nebula.

Evolutive tracks suggest an initial mass of $48 \pm 6 M_{\odot}$, and it's present mass is estimated to be at the most $40 M_{\odot}$, but lower masses ($\sim 30 M_{\odot}$) are also reported in literature (Lamers et al. 1983, Lamers et al. 1985, and Turner et al. 1999). However, the fine spatial structure of this large amount of excreted matter remains to be detailed. P Cyg's relative proximity (~ 1.8 kpc, Lamers et al. 1983) represents an opportunity to observe its radiatively driven mass loss from the starting point out to the interstellar medium. Indeed, at 1.8 kpc, the central star radius ($76R_{\odot}$) corresponds to a tiny angle of 0.2 milliarcsecond (mas) but the H_{α} emitting region extends over several tens of arcsec, and radio emission seems to attain at even larger scales (Meaburn et al. 1999). The optical and radio observations depict so far an essentially clumpy distribution of matter both at large (Taylor et al. 1991, Nota et al. 1995) and small scales (Skinner et al. 1998, Vakili et al. 1997), with temporally variable emission (Skinner et al. 1997). These imaging observations remain sparse and can loosely constrain the spatial and/or temporal evolution of the clumps in the nebula. Moreover, in the optical wavelengths, the star to the envelope brightness ratio remains an obstacle for studying the central star immediate environment. In this paper we report an attempt to observe the H_{α} circumstellar environment of P Cyg during an AO run at OHP observatory on October 1997 using short exposures collected with a photon-counting camera.

The paper is organized as follows. In section 2, we describe the AO+imaging instrumentation used for this study as well as data reduction and calibration procedures. Section 3 describes the image reconstruction in which particular efforts have been made to test the validity of the PSF. The last section makes a critical discussion of our found-

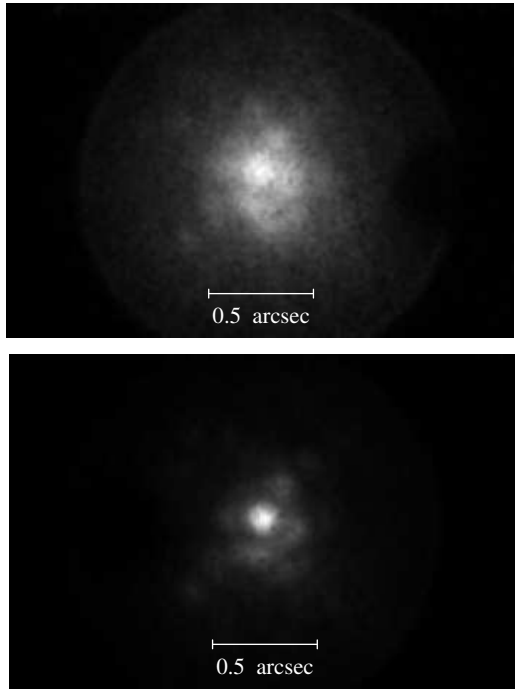


Fig. 1. H_{α} long exposures of P Cyg (top) and the reference star 59 Cyg (bottom) recorded with the CP20 camera at OHP during October 4th 1997 using the AO system BOA from ONERA through a filter ($\Delta\lambda=10\text{nm}$). The images are smoothed using a moving average window of 4×4 pixels. Note that the theoretical angular resolution of the 1.52m telescope at 6563\AA ($1.22\lambda/D=0.110$ arcsec) is closely reached (broken first Airy ring is visible on 59 Cyg) whilst for P Cyg a more complex and resolved structure can be suspected.

ing, and attention is given on the perspectives opened by the emergencies of new high angular resolution techniques. A need arise for a coordinated campaign for a global approach of P Cyg, and LBVs environment.

2. Journal of observations

2.1. Instrumentation

P Cyg was observed, in the context of a dark-speckle run (Boccaletti et al. 1998). The AO bench of the ONERA (Office National d'Etudes et de Recherches Aérospatiales) was installed at the Coudé focus of the 1.52m telescope. The 90 actuators of BOA and its 1 kHz closed loop bandwidth enable a compensation of atmospheric turbulence in visible light (Conan et al. 1998) and provide typical Strehl ratio of 10% to 30% depending on seeing conditions.

The restored wavefront feeds a dark-speckle optics designed to detect faint companions around bright objects. The beam is then focused onto the detector with an $f/976$ aperture, giving a fine pixel sampling of 144 pixels/arcsec or 0.007arcsec/pixel (this oversampling of the images was

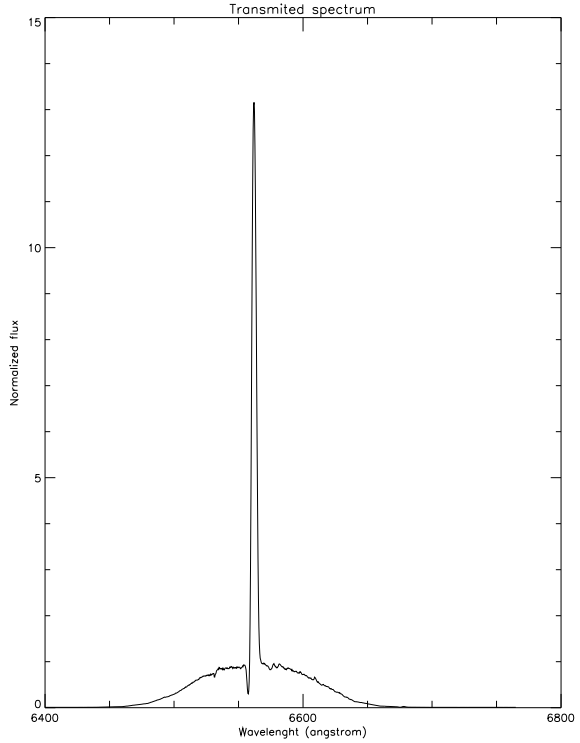


Fig. 2. Synthetic representation of the H_{α} region of P Cyg multiplied by the filter transmission used for the adaptive optics imaging of P Cyg. The same filter was used for 59 Cyg. About 45.6% of the transmitted light originates from the line continuum.

imposed for the dark-speckle experiment). The detector is a cooled CP20 photon-counting camera (Abe et al. 1998) allowing single photon detection with a very low dark count ($< 5.10^{-3}\text{ photon/pix/s}$). The quantum efficiency of CP20 is less than 10% at 700nm .

Near diffraction-limited images of P Cyg ($m_v = 4.81$, $S_p = B1Ia+$) and 59 Cyg ($m_v = 4.74$, $S_p = B1.5V$) have been obtained (Fig. 1) using a broadband H_{α} filter ($\lambda_0 = 6563\text{\AA}$, $\Delta\lambda = 100\text{\AA}$) (Fig. 2).

2.2. Data analysis

The data consist in two sequences of 20 ms short exposures, for respectively P Cyg, and the reference star 59 Cyg of similar magnitude and spectral type. In a preliminary step, the short exposures recorded by CP20 were cleaned for photon-centroiding electronic artifacts and then co-added to generate an equivalent long exposure of 99s for P Cyg and 370s for 59 Cyg. Despite the Coudé configuration of the 1.52m telescope, rotation of the field between the two sequences was found negligible. We checked for non-linear effects introduced by the so-called photon-centroiding hole and camera saturation (Thiébaut 1994). It appears that the incoming flux is much below the saturation limit, the double-photon oc-

Table 1. Turbulence characteristics derived from the wavefront sensor data of the adaptive optics system. Atmospheric parameters are given for the visible band.

| Star name | P Cyg | 59 Cyg |
|---|----------|----------|
| Time | 20:30 TU | 21:23 TU |
| Average intensity in sub-apertures (photons) | 51.567 | 42.830 |
| r_0 (cm), open loop calculated with L_0 | 5.83 | 5.92 |
| r_0 (cm), open loop calculated with L_0 and Zernike coef. | ~5.4 | ~5.4 |
| L_0 (m) | 2.96 | 2.57 |
| Zernike coef. (2,3), σ^2 (rad ²) | 70 | 40 |
| Zernike coef. (4,44), σ^2 (rad ²) | 10 | 9 |

cence is absent. The total number of detected photons for the two images are very similar: 481563 for P Cyg and 416309 for 59 Cyg. A coherent peak and a broken ring, featuring a triple coma aberration, are clearly visible, but 59 Cyg's image is sharper, indicating that P Cyg's envelope is possibly resolved. This is quite visible in Fourier space, as shown in Fig. 3. The envelope of P Cyg clearly appears as the well resolved low frequency part in the visibility curve. High angular information is obtained up to about 80 % of the cut-off frequency. The visibility curve is indeed clearly dominated by noise beyond that limit.

Since 59 Cyg has been observed 53 minutes later than P Cyg, a variation of atmospheric conditions and/or a poor correction could be responsible of a noticeable change in the Point Spread Function (PSF) shape. From open/close loop data recorded by the wavefront sensor of BOA, seeing conditions have been derived by one of us (F.C.) : intensity in sub-apertures, Fried parameter evolution, noise evolution, Zernike coefficient variance evolution, etc... Some of these relevant parameters are summarized in Table 1 for both stars. In particular the Fried parameter (r_0) exhibits no temporal variation and remains stable around 5.4cm between the 2 data sequences. Also, high order correction (Zernike coef. (4,44)) have similar variances in both cases, indicating similar adaptive mirror corrections for P Cyg and 59 Cyg. The largest difference appears for the tip-tilt corrections (Zernike coef. (2,3) of the Table 1). However we confirm that during the observations no saturation was detected, and we expect these modes be correctly compensated for both stars. Furthermore, parameters such as turbulent layers altitude, mean isoplanetic angle and wind velocity indicate a very good stability of the atmospheric conditions during the two records.

Moreover, the photon flux stability can be checked on the short exposures statistics. For 59 Cyg, the flux is stable with a perfect Poisson variance. P Cyg's behavior is roughly the same, except some localized empty exposures,

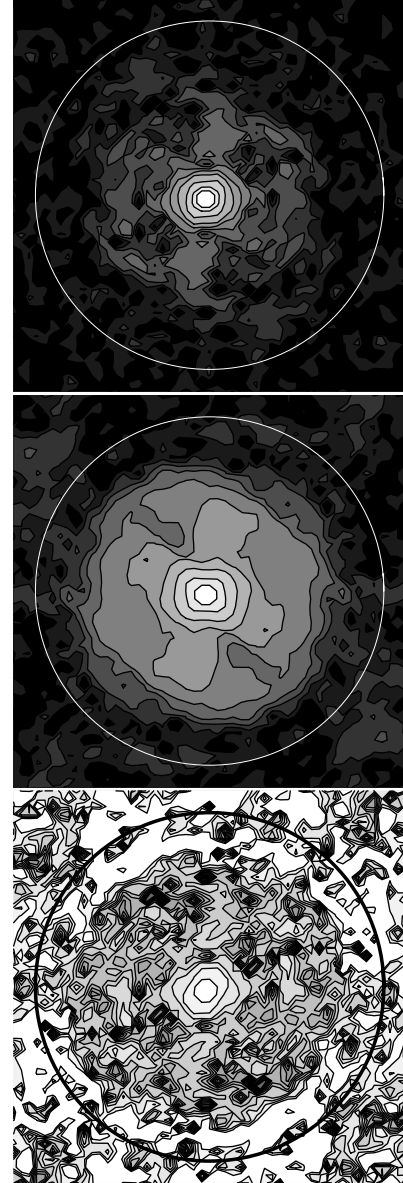


Fig. 3. Representation in contour plots of the modulus of the Fourier transform of P Cyg (top), 59 Cyg (middle) and their ratio, the visibility curve of P Cyg (bottom). The zero frequency is at the center of the images. The representations are in logarithmic scale. The circle gives the theoretical cut-off frequency of the telescope.

due to electronic saturation, which have been removed. This preliminary analysis permits to assume that 59 Cyg can be confidently considered as P Cyg's PSF and a successful deconvolution becomes possible.

3. Image reconstruction

3.1. Deconvolution of the raw image of P Cyg

A deconvolution of the image of P Cyg using 59 Cyg as the PSF has been made using basically the iterative Richardson-Lucy algorithm (RL) (Richardson 1972, Lucy 1974) to which some improvements have been applied as we shall describe thereafter. To improve the result, a pre-processing of the image was first performed. All images were smoothed using a moving average window of 4×4 pixels. To get rid of the effects of the coronagraphic mask (clearly visible in Fig. 1 at the right of P Cyg's image), only a central region of 0.9×0.9 arcsec of the smoothed images was conserved. To make the deconvolution procedure faster, the number of points of the images was further reduced by a factor 16. The resulting images of 32×32 pixels remain correctly sampled (0.028 arcsec compared with the theoretical Shannon limit of 0.044 arcsec for the 1.52m telescope operated at 656.3nm).

The RL algorithm was then applied to these pre-processed images using the well-known iterative procedure:

$$x^{k+1}(r) = x^k(r) \cdot h(-r) \otimes \frac{y(r)}{h(r) \otimes x^k(r)} \quad (1)$$

where \otimes is the convolution symbol, r denotes the two-dimensional spatial position, $y(r)$ denotes the image of P Cyg, $h(r)$ the image of 59 Cyg taken as the PSF, and where $x^k(r), x^{k+1}(r)$ are the reconstructed images at the iteration k and $k+1$.

To limit the instability that appears in the solution, due to the amplification of noise, we stop the iteration number by using a comparison between the Fourier Transform of the reconstructed object at the iteration k and the Fourier transform of the image reconstructed by a Wiener filter (Lantéri et al. 1998, Lantéri H., Soummer R. et al. 1999). The main difficulty is then shifted to a correct determination of the Wiener filter. The comparison lead to choose an iteration number of 245. The result of the deconvolution is given both in gray levels and in contour plot in Fig. 4. To make the envelope clearly visible, the contour levels are not equally spaced. The general pattern is that of a bright star, not resolved by the 152 cm telescope, surrounded by an extended envelope with bright spots.

These same results were obtained when we used for the reconstruction the RL algorithm regularized by a Tikhonov term, and more specially using the Laplacian operator (Lantéri H., Roche M. et al. 1999). The result of this deconvolution is presented in Fig. 5 for the iteration 250 with a regularization factor equal to 0.01. Neglecting the fine structure of the envelope, a normalized circular average of the image centered on the star may be fitted by the sum of two Gaussian curves, of the form: $ae^{-b|r|^2} + (1-a)e^{-b'|r|^2}$ where $a \simeq 0.85$, $b \simeq 618.2$ and $b' \simeq 25.9$ if we express r in arcsec. This corresponds to an equivalent width of the envelope of about 0.4 arcsec ($\frac{2}{\sqrt{b'}}$). The radial curve is shown in a semi-logarithmic scale in Fig. 6. In this model

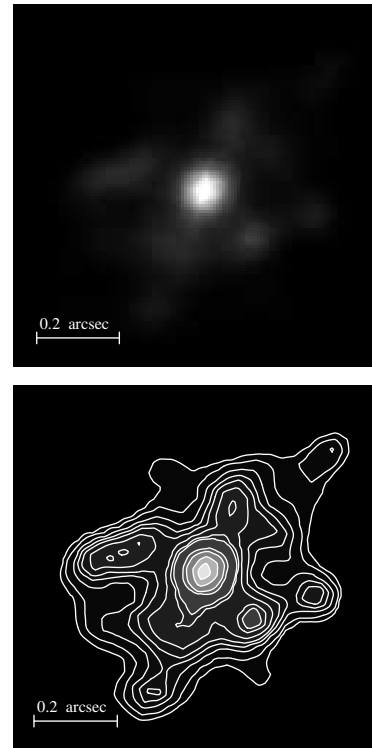


Fig. 4. Reconstructed image of P Cyg with the RL algorithm stopped at iteration 245. Top: Representation in gray levels in a linear scale. Bottom: Representation in contour plot. Contours levels are not equally spaced and correspond to : 100, 80, 60, 40, 30, 15, 12.5, 9, 6.5, 5, 3.5, 2, 1.2 percent of the image's maximum. North is at the top and East is at the right of the images. This corresponds to a rotation of 104.7° clockwise with regards to Fig. 1.

the total integrated flux produced by the envelope ($r = (1-a)b/ab'$) was found to be about 4 times larger than the one produced by the central star. This ratio is not an absolute parameter; it depends of course of the spectral bandwidth of the experiment (Fig. 2).

We may conclude from this first analysis that the envelope of P Cyg is well resolved by the central core of the PSF of the 1.52 m telescope, corrected by the adaptive optics system. However, the envelope remains comparable in size with the residual halo of the PSF. This assumes at least that we are free of anisoplanatism problems (Fusco et al. 2000); this absence of variation allows the use of conventional deconvolution methods.

The question then may arise whether some of the fine structures we discovered in this envelope may be due to artifacts of the reconstruction process. Among others problems, a very important one is a possible variation of the PSF during the experiment (from P Cyg to 59 Cyg), as discussed recently by Harder and Chelli (Harder and Chelli 2000). These authors show that a local non-stationary turbulence may produce strong residual



Fig. 5. Reconstructed image of P Cyg with the RL algorithm regularized by the Laplacian operator. Contours levels are not equally spaced and correspond to: 100, 80, 60, 40, 30, 15, 12.5, 9, 6.5, 5, 3.5, 2, 1.2 percent of the image's maximum. North is at the top and East is at the right of the image.

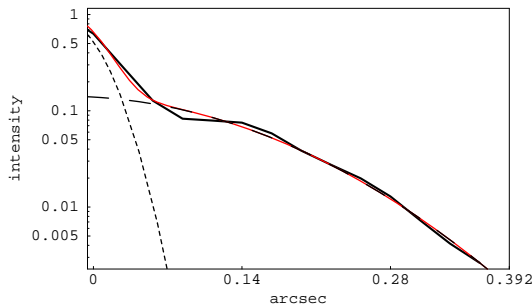


Fig. 6. Thick line: Radial profile of the object reconstructed by RL stopped at iteration 245 (image normalized to one). Dashed lines: Gaussian curves. Thin line: Sum of the two Gaussian curves. Intensity is in logarithmic scale.

aberrations (clearly visible in the first diffraction ring of their figure 17). At worst, can we imagine that the observed structures in our image result only from variations in the PSF, from P Cyg to 59 Cyg?

A comparison between the reconstructed image and the PSF is made in Fig. 7. To make the structures more visible, we used a representation similar to that of Harder and Chelli (Harder and Chelli 2000). The images are negatives of intensities and the representation uses threshold and saturation. Doing so, a strong (white) secondary maximum appears in the image of P Cyg, and two lower ones remain far away from the core. Moreover, Fig. 7 clearly evidences that the central (white) surface of the reconstructed object is larger than that of the PSF (this will be interpreted in the next section as an effect of the envelope). It seems difficult to explain that such a structured image is only the result of variations of the PSF. However, it is also difficult to ascertain that our reconstructed image is free of any residual error (much more data would

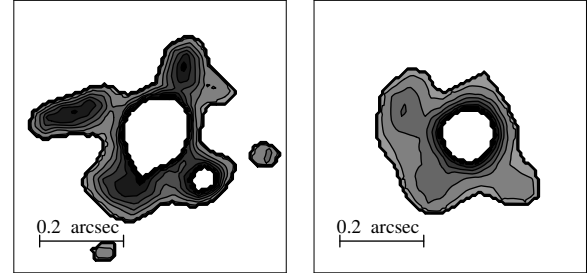


Fig. 7. Representation at the same scale of the reconstructed image of the Fig. 5 (left) and of the PSF (right) in contour plot. The white parts are due to the threshold and the saturation applied to both images: intensities lower than 6 % and higher than 15 % of the maximum are made white. North is at the top and East is at the right of the images.

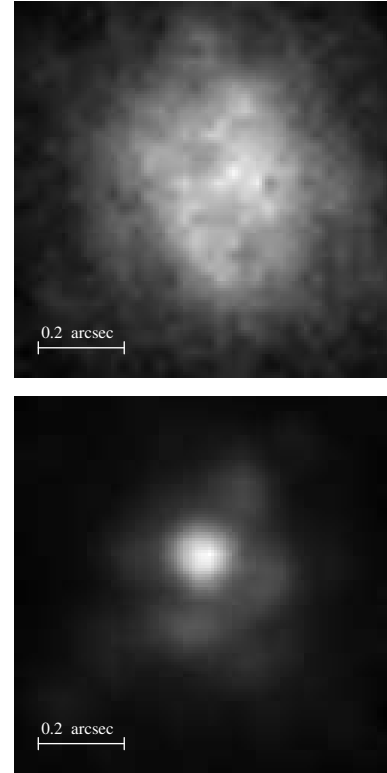


Fig. 8. Representations in gray levels of the residual blurred envelope $e(r) \otimes h(r)$ (top) and of the fraction $\gamma h(r)$ of the image of 59 Cyg subtracted from P Cyg (bottom). The sum of these two images gives back the observed image of P Cyg. The orientation is that of Fig. 1.

have been necessary for that). To strengthen our confidence in the fine details of the reconstructed image of the envelope, we have implemented a series of processing and tests. They are described in next sections 3.2 and 3.3, and in the Appendix.

3.2. Deconvolution of the envelope - alone of P Cyg

We have further processed the data assuming that P Cyg observed in H_{α} may be fairly represented by an unresolved star surrounded by an extended envelope. Let us write P Cyg as $e(r) + \gamma\delta(r)$, where $e(r)$ is the envelope and γ the relative intensity of the star defined by the Dirac function $\delta(r)$. The observed image is then modeled as $y(r) = e(r) \otimes h(r) + \gamma h(r)$. We have implemented a somewhat heuristic procedure that consists of subtracting $\gamma h(r)$ from $y(r)$ to obtain $e(r) \otimes h(r)$. The procedure has some similarity with what is made in the algorithm CLEAN (Högbom 1974), and the algorithm of Lucy (Lucy 1994). In practice, it consists of subtracting an appropriate fraction of the image of 59 Cyg correctly shifted from P Cyg. The parameters of this subtraction are determined to leave a smooth pattern for $e(r) \otimes h(r)$, with no remaining bump or hole due to the unresolved star. We found that a fraction $\gamma = 20\%$ of the PSF ($h(r)$), shifted of a displacement (X = -0.3 pixels, Y = +1.3 pixels) was to be subtracted from P Cyg ($y(r)$). This was done using an interpolation of the images with Mathematica (Wolfram S. 1999). Fig. 8 shows the residual blurred envelope $e(r) \otimes h(r)$ (top) and the fraction of the PSF subtracted to the image of P Cyg $\gamma h(r)$ (bottom). This procedure, performed independently of the above deconvolution and parametric estimation of the star plus envelope, lead also to the same ratio 4 for the energy of the envelope relative to the central star.

We then processed the residual blurred envelope $e(r) \otimes h(r)$ using the same RL algorithm stopped at the same iteration number 245. The result is given both in gray levels and in contour plot with linear contour spacing in Fig. 9. The image of the envelope is fully consistent with what was obtained in the raw deconvolution of Fig. 4. The bright spots are all found at the same position. Moreover, there is a bright spot very close to the star clearly visible in this representation in the South-West direction; it was only perceptible as a small deformation of the central star in Fig. 4.

3.3. Analysis of the quality of the deconvolution

We have implemented a few more computations to check the quality of the results we give in this paper. The whole deconvolution procedure was also performed using the Image Space Reconstruction Algorithm (ISRA) (Daube-Witherspoon et al. 1986) instead of the RL algorithm. The comparison with the image reconstructed by the Wiener filter leads us to the iteration 303. The reconstructed image is presented in Fig. 10. The two algorithms gave almost the same results which reinforced us in the confidence we have in the deconvolution results given in this paper.

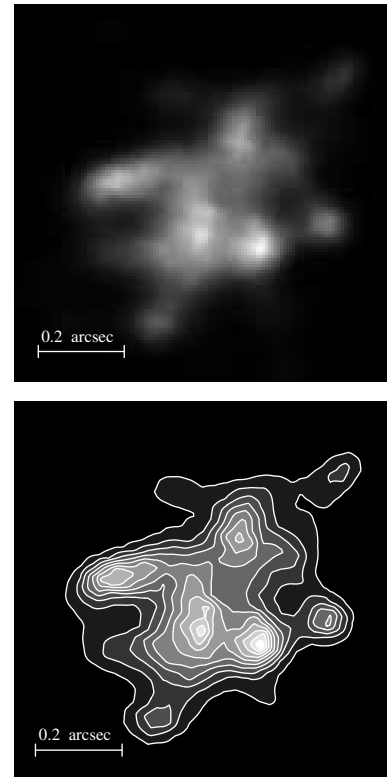


Fig. 9. Image reconstruction of the envelope of P Cyg in gray levels (top) and in contour plot (bottom). Contours levels are equally spaced. North is at the top and East is at the right of the images.

At that point we may conclude that the deconvolution was carried out taking into account the problem of noise; we also made use of an a priori model, by assuming that P Cyg was the sum of an unresolved star and an envelope. A significant question remains: up to what precision can we trust 59 Cyg as an accurate PSF for P Cyg? Several elements enable us to give a positive answer to that question: the seeing conditions were similar for both observations, and we found the same ratio of the flux envelope/star (about 4) before and after deconvolution. It would have been very convincing to have a series of observations of P Cyg and a reference, eventually with different seeing conditions, and have all the results that converge towards a unique solution. In fact, we made an elementary test that consisted in dividing the long exposure of P Cyg in two sequences. The same operation was applied to 59 Cyg. We have then made a deconvolution of these four resulting images. The results are very similar to those obtained with the deconvolution presented in Fig. 4 and are not reproduced here. In an alternative way, we give in the appendix the results of a series of additional tests that tend to confirm 59 Cyg as a correct PSF.

At that point, we think that we obtained all that allowed the present data. Of course, futures observations, with



Fig. 10. Reconstructed image of P Cyg with the ISRA algorithm stopped at iteration 303. Contours levels are not equally spaced and correspond to: 100, 80, 60, 40, 30, 15, 12.5, 9, 6.5, 5, 3.5, 2, 1.2 percent of the image's maximum. North is at the top and East is at the right of the image.

possibly a larger telescope, will be very usefull to confirm our first results and to further precise the morphology of this object.

4. Discussion

The present work follows a long series of observations to track the history of P Cyg's giant eruptions in 1600 and 1655. Following the first attempts in this direction (Feibelman 1995), it clearly appeared that the star to its nebula brightness ratio constitutes a challenging obstacle for the optical mapping of the nebular morphology. Indeed only few observations, with heterogeneous angular resolutions are reported in the literature. Leitherer and Zickgraf (Leitherer et al. 1987) first published the detection of P Cyg's extended nebulosity using CCD imaging. Later, Johnson et al. (Johnson et al. 1992) reported the detection of forbidden emission lines due to nitrogen enriched material at 9 arcsec. The first coronagraphic imaging of P Cyg from the ground was obtained by Barlow et al. (Barlow et al. 1994) from high resolution long-slit data. Barlow and co-workers discovered the presence of a 22 arcsec nearly circular shell which presents bright condensations of about 2 arcsec wide, mostly in the North (their plate scale is of 0.255 arcsec per pixel where a 4.3 arcsec occulting strip was used). STScI coronagraph imaging, using a 4.8 arcsec occulting disk, shows almost the same features (Nota et al. 1995). From another point of view P Cyg constitutes an ideal target for testing new and different imaging techniques. Among these there are the spectral-line image sharpening techniques SCASIS (de Vos 1994), the AMOS adaptive optics observations (Morossi et al. 1996), and occulting mask imaging (4 arcsec) with the new MOMI instrument for wide field imaging (O'Connor et al. 1998). In the latter case

the authors suggest highly asymmetrical features at 3-4pc from the star (7') probably associated to previous mass-loss events (Meaburn et al. 1999). At the same time, radio imaging now offers approximately the same panel of field and spatial resolution as optical imaging making the comparison of optical and radio maps possible. Indeed, sounding different scales in radio wavelength can easily be achieved by changing the baseline configuration of radio arrays (Skinner et al. 1998). Using this possibility Skinner and co-workers have compared radio maps to Barlow's coronagraphic image of P Cyg (Barlow et al. 1994). These authors claim that the emissive regions in radio and visible are roughly the same, although this comparison is further complicated by the coronagraphic mask and the telescope diffraction pattern. They conclude that both radio and optical maps exhibit the same details having the same physical origin: i.e. dense clumps overtaken by the faster wind and heated by shocks.

Low and intermediate spatial resolution images suggest a global spherical expanding envelope but clumpiness is present in each case. This trend is also present at higher spatial resolution of the 250km MERLIN centimetric network (Skinner et al. 1997) approaching the submilliarcsecond observations of the GI2T optical interferometric (Vakili et al. 1997).

In this context our present reconstructed image of P Cyg's environment in H_{α} presents, as expected, strongly clumped features within the 1 arcsec field of view (0.011pc with $D=1.8\text{Kpc}$). More than 6 enhanced emission clumps are counted with our 0.05 arcsec spatial resolution in a nearly 0.6 arcsec region superimposed to the unresolved central star. The mean size of the clumps is roughly 0.08 arcsec which is the angular limitation of the 152cm OHP telescope. These results agree well both in size and morphology with MERLIN observations, at nearly the same resolution. The typical diameter of emitting regions for MERLIN is 0.4 arcsec (0.13 arcsec for the core), and amazingly comparable to the optical structures (Fig. 9). In this same figure, a North-East/South-West preferential axis appears in the H_{α} image due to the grouping of the clumps, the distribution being otherwise rather uniform. The same orientation was also pointed out in SCASIS observations at a lower spatial resolution (de Vos 1994). Note that in our reconstructed image a bright feature is located at 80 mas South-East of the central star. We can speculate on its relation to the local strong emission discovered at 0.8 mas from the star in august 1994 by the GI2T interferometer (Vakili et al. 1997) although the E-W absolute position of the latter emission was not given by this instrument. If this scenario holds, this position some 3.2 years after implies a projected velocity around 110km/s. Taking into account the radial velocity and uncertainties $208\pm78\text{km/s}$ obtained by Vakili et al. (Vakili et al. 1997), this projected velocity is to be expected for a clump nearly on the line of sight ejected three years earlier with the terminal velocity, and thus, compat-

ible with the GI2T observations. Although the possible physical relation of 1994 blob and 1997 clump remains to be robustly settled, interferometric and AO imaging repeated in the future, should enlight such scenario.

At the present, only radio observations by Skinner et al. (Skinner et al. 1997) present confident temporal variations. In the two 6-cm MERLIN images taken in a 40 days interval, impressive changes were observed, corroborated by VLA observations. In the observed region, the wind velocity suggests a 2 years dynamical time scale, which can hardly be compared to the 6-cm flux variations. On the other hand, the recombination time scale for hydrogen atoms ($1.210^5/n_e$ in years) is shorter, but not sufficient, ~ 160 days considering a characteristic n_e of 2.810^5 cm^{-3} at 0.07 arcsec. This short time scale puts strong constraints on the electron density, which has to be four times larger than the surrounding envelope material. The clumpiness can explain such a time evolution if the structures are sufficiently small and dense, or if the shocks between the wind and the clumps are strong enough. The question is whether increasing resolution would reveal the same clumpiness, and if activity observed in optical and radio wavelengths are closely correlated.

Some questions arise. How can these small scale clumps be related to the 2 arcsec ones observed in the Barlow's images at 3 arcsec from the star? How can they survive over such a long distance? Do they reappear at the location we detect them?

A challenging issue is now understanding the connection between the different spatially resolved structures and their scales which needs the monitoring of the clumpiness from the star to the interstellar medium, and constrains the mass ejection dynamics. Therefore, our present observations are the first attempt to prove that an optical monitoring of the clumpiness in inner region of P Cyg's mass loss is observationally feasible. As previously pointed out (Vakili et al. 1997), the intermediate regions of P Cyg's wind, from a few stellar radii to a few parsecs can be sounded by means of AO plus coronagraphic imaging from the ground, in relation with radio observations. The dynamical time scale for optical interferometry is around the month, but a temporal monitoring of P Cyg by this technique requires both higher sensitivity and larger numbers of baseline orientations due to the complex structures which occur at different scales. For larger distances, the recombination time scale in the clumpy wind should produce large effects as detected in radio, and AO becomes the perfect technique to follow such activities. The brightness of P Cyg and its evolutionary time scale allow the development of a multi-site and multi-wavelength observations campaign, using AO, optical and radio interferometry to get a unified picture of P Cyg's environment physics.

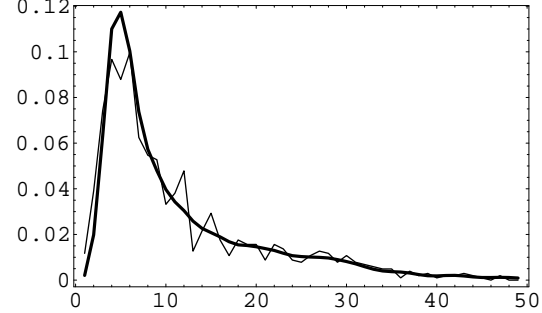


Fig. A1. Thick line:Poisson-Mandel transform $P(y)$ of $P(b)$ calculated using relation A1. Thin line: Histogram of the values of $y(r)$. A good agreement between the two curves is observed.

Appendix A: Tests on the PSF

We have made a series of tests that tends to strengthen our confidence in the 59 Cyg's image as a correct PSF for P Cyg. These tests are negative tests in that sense that if the PSF fails to succeed one, it should be rejected as a bad PSF.

Let us assume that 59 Cyg is a good unbiased representation of the true PSF $h(r)$. Differences between the blurred reconstructed image $b(r) = h(r) \otimes x(r)$ and the observed data $y(r)$ must then be dominated by statistical noise fluctuations, with no bias term. In this relation $x(r)$ is our best reconstructed image, as shown in Fig. 4, and $h(r)$ the PSF 59 Cyg of Fig. 1 of the body of the paper. We assume that the noise comes from a photo-detection process, and that $y(r)$ is a realization of the Poisson process of mean $b(r)$.

A.1. Test 1: Poisson-Mandel transform

The first test we have performed is a basic one, not very sensitive to the exact value of $h(r)$, but that must be verified in any case. Let us denote y and b the values taken by $y(r)$ and $b(r)$. The total probability theorem (Papoulis 1984) allows us to write the unconditional probability $P(y)$ of $y(r)$ as the sum of $P(y/b) \times P(b)$ for all b values. For the Poisson process, the conditional probability of y assuming b is $P(y/b) = \frac{b^y}{y!} \exp -b$ where y is an integer (the number of photons) and b a continuous value.

As a consequence, $P(y)$ is the Poisson-Mandel transform (Mandel 1959, Mehta 1970) of $P(b)$:

$$P(y) = \int_0^{\infty} P(b) \frac{b^y}{y!} \exp -b \, db \quad (\text{A1})$$

We have verified that our data correctly obeys relation A1. We have taken for $P(b)$ the histogram of $b(r)$, applied the above transformation and compared the result $P(y)$ with the direct histogram of the values of $y(r)$. The comparison is shown in Fig. A1. The results are consistent with the data.

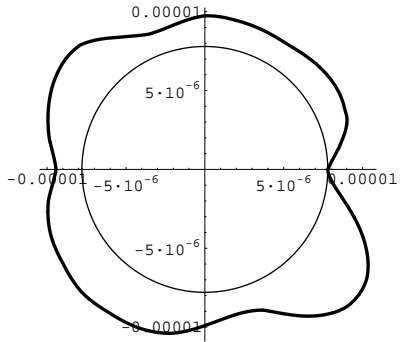


Fig. A2. Thick line: Polar plot of the Euclidean distance between $y(r)$ and $b_\theta(r)$ for θ varying between 0 and 2π . Thin line: Circle with a radius of the minimum of the Euclidean distance between $y(r)$ and $b_\theta(r)$. The minimum of the Euclidean distance is obtained for $\theta = 0$.

A.2. Test 2: Rotations of the true PSF

The second test we have performed was to check the correctness of the small departures from circular symmetry of 59 Cyg. We use as the PSF $h_\theta(r)$ an image of 59 Cyg rotated of an angle θ . Then the deconvolution procedure is carried out as previously and leads to an image $x_\theta(r)$. The blurred image $b_\theta(r)$ is obtained as the convolution of $x_\theta(r)$ and $h_\theta(r)$, and we finally compute the Euclidean distance between $y(r)$ and $b_\theta(r)$. The results are shown in Fig. A2 in a polar plot for θ varying from 0 to 2π . The original PSF gives the best result. If the deviation from circular symmetry were purely random, the goodness of the deconvolution would not be affected by this rotation. Secondary minima of the curve appear for apparent symmetries of the PSF.

Representations of the difference between $y(r)$ and $b_\theta(r)$ are shown in Fig. A3. For the sake of clarity we have represented the sign of the difference $y(r) - b_\theta(r)$. For $\theta = 0$, we get a speckle-like pattern, roughly uniform over the whole image. For other values of θ , this difference shows large patterns that indicates regions over which $b_\theta(r)$ does not correctly matches $y(r)$. These trends clearly show that $h_\theta(r)$ for $\theta \neq 0$ is a biased version of $h(r)$.

As a conclusion, 59 Cyg passed the tests and could not be rejected as a bad PSF.

Acknowledgements. We wish to acknowledge A. Labeyrie for having encouraged the present work. P Cyg's observations were done using the BOA Adaptive Optics provided by ONERA to us. The manuscript benefited from discussions and critics of J.P. Véran, J. De Freitas Pacheco, G. Ricort and the GI2T team.

References

Abe L., Vakili F., Percheron I., Hamma S., Ragey J.P., Blazit A., 1998, in proceedings of the conference "Catching the

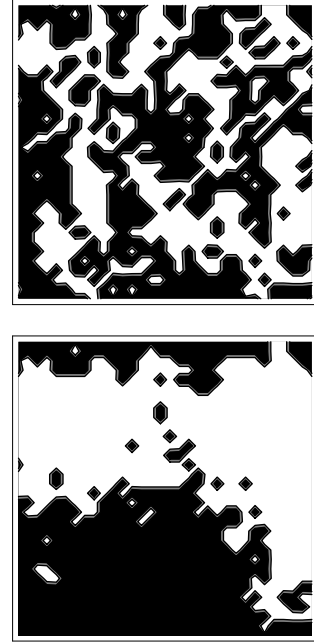


Fig. A3. Representation of the sign of the difference $y(r) - b_\theta(r)$ for no rotation of the PSF (top) and for a rotation of $\pi/2$ (bottom). This later image is not a particular case, and is characteristic of what can be obtained when the PSF is rotated.

perfect wave" (Albuquerque, june 1998)
 Barlow M.J., Drew J.E., Meaburn J., Massey R.M., 1994, MNRAS, 268, L29
 Boccaletti A., Moutou C., Labeyrie A., Kohler D., Vakili F., 1998, AASS 133, 395-492
 Conan J.M., Mugnier L., Fusco T., 1998, in proceedings of the Adaptive Optics and Applications, SPIE 3126
 Daube-Witherspoon M.E. and Muehllehner G., 1986, I.E.E.E. Trans. Med.Imaging, MI-5, 61-66
 de Groot M.J.H., Lamers H.J.G.L.M., 1992, Nature, 355, 422
 de Vos C.M., 1993, Ph. D. Thesis, oiks.book
 de Vos C.M., 1994, IAUS, 158, 419
 Feibelman W. A., 1995, JRASC, 89, 3
 Fusco T., Conan J.-M., Mugnier L.M., Michau V. and Rousset G., 2000, AASS, 142, 149-156
 Harder S. and Chelli A., 2000, AASS, 142, 119-135
 Högbom J.A., 1974, AASS, 15, 417-426
 Johnson D.R.H., Barlow M.J., Drew J.E., Brinks E., 1992, MNRAS, 255, 261
 Lamers H.J.G.L.M., de Groot M.J.H., Cassatella A., 1983, A&A, 128, 299-310
 Lamers H.J.G.L.M., Korevaar P., Cassatella A., 1985, A&A, 149, 29
 Lantéri H., Soummer R., Aime C., 7-11 September 1998, ESO/OSA Topical Meeting on Astronomy with Adaptive Optics, Sonthofen, Germany
 Lantéri H., Roche M., Cuevas O., Aime C., 20-24 September 1999, ESO/SPIE Symposium on Remote Sensing, Florence, Italy
 Lantéri H., Soummer R., Aime C., 1999, AASS, 140, 235-246
 Leitherer C., Zickgraf F.J., 1987, A&A, 174, 103

Lucy L.B., 1974, AJ, 79, 745-754

Lucy L.B., 1994, The restoration of HST images and spectra
II. Space Telescope Institute, Hanisch R.J. and White R.L.
eds, 79-85

Mandel L., Proc. Phys. Soc., 74, 233

Meaburn J., López J.A., O'Connor J., 1999, ApJ, 516, L29

Mehta C.L., 1970, Progress in Optics, 3, 399-428

Morossi C., Franchini M., Ragazzoni R., et al., 1996, SPIE,
2828, 301

Nota A., Livio M., Clamplin M., Schulte-Ladbeck R., 1995,
ApJ, 448, 788

O'Connor J.A., Meaburn J., Bryce M., 1998, MNRAS, 300,
411

Papoulis A., 1984, McGraw-Hill Series in Electrical Engineering,
Second Edition, 30

Richardson W.H., 1972, J.Opt.Soc.Am, 62, 55-59

Skinner C.J., Exter K.M., Barlow M.J., Davis R.J., Bode M.F.,
1997b, MNRAS, 288, L7

Skinner C.J., Becker R.H., White R.L., Exter K.M., Barlow
M.J., Davis R.J., 1998, MNRAS, 296, 669

Taylor M., Nordsieck K.H., Schulte-Ladbeck R.E., Bjorkman
K.S., 1991, AJ, 102, 1197

Thiébaut E., 1994, A&A 284, 340-349

Turner D., Welch G., Horsford A. et al., 1999, JRASC, 93, 186

Vakili F., Mourard D., Bonneau D., Morand F., Stee P., 1997,
A&A 323, 183-188

Wolfram S., 1999, The Mathematica book, Fourth Edition,
Cambridge University Press